Virtual photon emission from a quark-gluon plasma

S. V. Suryanarayana*
Nuclear Physics Division, Bhabha Atomic Research Centre, Trombay, Mumbai 400 085, India
(Received 1 May 2007; published 9 October 2007)

We present phenomenological formulas for virtual photon emission rates from a thermalized quark-gluon plasma (QGP) that include bremsstrahlung and annihilation with scattering (AWS) mechanisms along with the Landau-Pomeranchuk-Migdal (LPM) effects. For this purpose we follow the approach of generalized emission functions (GEF) for virtual photon emission, we showed earlier for a fixed temperature and strong coupling constant. In the present work, we extend the LPM calculations for several temperatures and strong coupling strengths, photon energies (q_0), photon mass (Q^2), and quark energies (p_0). We generalize the dynamical scaling variables, x_T, x_L, for bremsstrahlung and AWS processes that are now functions of variables $p_0, q_0, Q^2, T, \alpha_s$. The GEF introduced earlier, g_T^b, g_T^a, g_L^b, g_L^a, are also generalized for any temperatures and coupling strengths. From this, the imaginary part of the photon polarization tensor as a function of photon mass and energy has been calculated as a one-dimensional integral over these GEF and parton distribution functions in the plasma. By fitting these polarization tensors obtained from GEF method, we obtained a phenomenological formula for virtual photon emission rates as a function of $\{q_0, Q^2, T, \alpha_s\}$ that includes bremsstrahlung and AWS mechanisms with LPM effects.

DOI: 10.1103/PhysRevC.76.044903 PACS number(s): 12.38.Mh, 13.85.Qk, 25.75.−q, 24.85.+p

Quantum chromodynamics (QCD) calculations on space time lattice [1] predict a transition from confined state in hadrons to a deconfined state of quarks and gluons above a temperature of 170 MeV or an energy density above 1 GeV/fm^3. In the relativistic heavy ion collisions at the Relativistic Heavy Ion Collider at Brookhaven National Laboratory, where the initial energy density is around 5 GeV/fm^3, such a transition to a deconfined state of matter is formed as shown by experimental measurements of several observables [2–5]; for details see the reviews in Refs. [6,7]. It is currently believed that this deconfined state consists of a strongly interacting quark-gluon plasma (sQGP), behaving nearly like a perfect liquid [7]. Among many observables, electromagnetic signals such as photon and low mass dilepton emission have been considered important as diagnostic tools to identify this state of matter. Photons and dileptons are emitted at various stages during the plasma evolution. The experimentally measured yields are obtained by convoluting the expansion history of the plasma with all the contributing processes to these signals from QGP as well as hadron phases. Therefore, understanding the physical processes in QGP phase that contribute to these signals and developing a phenomenological formulas that simulate the rates for these processes is of paramount importance. Study of thermal dilepton rates has evinced lot of theoretical interest in recent times. This is because the dilepton contribution can arise from the hard parton radiating off while traversing the QGP medium, known as the jet quenching process. It has been recently shown that this process gives contribution to dilepton emission and may be above the thermal dilepton emission rates from the thermalized QGP [8]. The current interest in dilepton emission comes from the lattice QCD calculations of the electromagnetic correlators and the lattice results for dilepton rates [9–13]. The results for zero three-momentum at two different temperatures were compared to the results of hard thermal loops (HTL) [14] method. The lattice rates are consistent with the HTL results at high energy, where as at lower energies, the lattice rates show a decrease as compared to the apparently diverging rates in the HTL method. If this decrease in lattice rates is due to lattice artifacts, then it gives a scope to verify agreement between lattice and perturbative results as well as a scope to verify agreement between different methods in lattice calculations, see Ref. [11]. Thus, the qualitative difference between these two results is currently under investigation. Recently, there has been a renewed interest in the dilepton emission rate in an ultrasoft energy limit [15]. In the soft limit, electromagnetic correlator can be related to the electrical conductivity [13,15]. However, the lattice calculations did not give unique answer to the value of the conductivity in the soft limit.

In this work, we present a study of virtual photon emission from thermalized QGP and a phenomenological formulas that reproduce these results. We concentrate on the Landau-Pomeranchuk-Migdal (LPM) effects [16,17] that arise due to the multiple scatterings of quarks in the QGP medium during a finite photon formation time. The LPM effects on real photon emission from QGP have been reported [18,19] and an empirical approach in [20]. For the case of virtual photon emission in QGP, the processes that contribute at $\alpha\alpha_s$ [21,22] and LPM effects [23] were well studied. (α, α_s are the electromagnetic and strong coupling strengths). In the HTL method these processes occur at the one-loop, two-loop, and higher-loop levels. At the one-loop level, Compton scattering ($qg \to q\gamma$) and quark and antiquark annihilation ($\bar{q}q \to g\gamma$) processes contribute to photon emission [21,22]. The processes bremsstrahlung and annihilation with scattering (AWS) contribute to photon emission at the two-loop level, as shown in Figs. 1(a) and 1(b). These are represented by $qi \to \gamma qi, \bar{q}qi \to \gamma gi$, where i represents quark, antiquark, or gluon. The processes in Figs. 1(a) and 1(b) arise when the

*snarayan@barc.gov.in or suryanarayan7@yahoo.com

photon self-energy is cut through the bulb on the exchanged gluon line in Fig. 1(c) when only a single gluon line is present in Fig. 1(c). It is expected that these two-loop processes should be of higher order in strong coupling strength α_s $(= g^2/4\pi)$. However, these contribute at leading order due to a collinear enhancement mechanism. For a collinear photon emission, the angle of internal quark line with the photon emission direction is of order g. Further, the exchanged gluon is soft (of momentum $\sim gT$), and the internal quark lines are nearly on shell. In the presence of the QGP medium, the collinear divergence of photon emission rate is regulated by the thermal masses. This mechanism of delicate cancellation of powers of g remains valid for any number of soft gluon exchanges during photon formation time [18,19] and the scattered quark lines are nearly collinear with the photon emission direction. Therefore, each new gluon line in the ladder brings a factor of $O(g^2/g^2)$, showing the need to sum the infinite set of such diagrams. These processes are represented by ladder diagrams as shown in Fig. 1(c) and these higher loop (ladder) processes also contribute at the same order $\alpha\alpha_s$. The resummation of these ladder diagrams leads to integral equations for transverse and longitudinal parts, whose solutions we will discuss in the following. In the photon emission calculations, the quantity of interest is the imaginary part of photon retarded polarization tensor $(\Im\Pi^{\mu}_{R\mu})$. The dilepton emission rates are estimated in terms of this $\Im\Pi^{\mu}_{R\mu}$, Bose-Einstein factor, and Q^2 as given by Eq. (1).

$$\frac{dN_{\ell^+\ell^-}}{d^4x d^4Q} = \frac{\alpha}{12\pi^4 Q^2(e^{q0/T}-1)}\Im\Pi^{\mu}_{R\mu}(Q) \tag{1}$$

$$\Im\Pi^{\mu}_{R\mu} = \frac{e^2 N_c}{2\pi}\int_{-\infty}^{\infty} dp_0[n_F(r_0)-n_F(p_0)] \otimes \int \frac{d^2\mathbf{p}_\perp}{(2\pi)^2}\left[\frac{p_0^2+r_0^2}{2(p_0r_0)^2}\Re\mathbf{p}_\perp\cdot\mathbf{f}(\mathbf{p}_\perp) + \frac{1}{\sqrt{|p_0r_0|}}\frac{Q^2}{q^2}\Re g(\mathbf{p}_\perp)\right], \tag{2}$$

where n_F in Eq. (2) represents the Fermi-Dirac distribution function of the incoming or outgoing quark energies $p_0, r_0 = p_0 + q_0$. Here q_0 is the photon energy and $Q = \sqrt{q_0^2 - q^2}$ is the photon mass. The $\Im\Pi^{\mu}_{R\mu}$, including LPM effects, is determined in terms of a transverse function $\mathbf{f}(\mathbf{p}_\perp)$ and a longitudinal part $g(\mathbf{p}_\perp)$, as given by Eq. (2). For the case of virtual photon emission having small virtuality, the transverse vector function $\mathbf{f}(\mathbf{p}_\perp)$ is determined by the AMY integral equation (Eq. (3)) [23]. In this integral equation, δE is an energy denominator and is interpreted as the inverse formation time of the photon. This energy transfer function $\delta E(\mathbf{p}_\perp, p_0, q_0, Q^2, T, \alpha_s)$ is given in Eq. (4). Here $\kappa_{\rm eff} = M^2_{\rm eff}/m_D^2$ and $M^2_{\rm eff} = M^2_\infty + \frac{Q^2}{q_0^2}p_0r_0$. $M^2 = g_s^2 C_F T^2/4$ is the thermal mass of a hard quark in the HTL approximation. $C_F(=4/3)$ is the Casimir in the fundamental representation of the gauge group $SU(N_c)$ with $N_c = 3$. Debye mass is given by $m_D^2 = g_s^2T^2(N_c + N_F/2)/3$ with N_F flavors. A tilde represents quantities in units of Debye mass; for details see Ref. [24]. In Eq. (3), $\tilde{C}(\tilde{\ell}_\perp)$ represents the collision kernel [26]

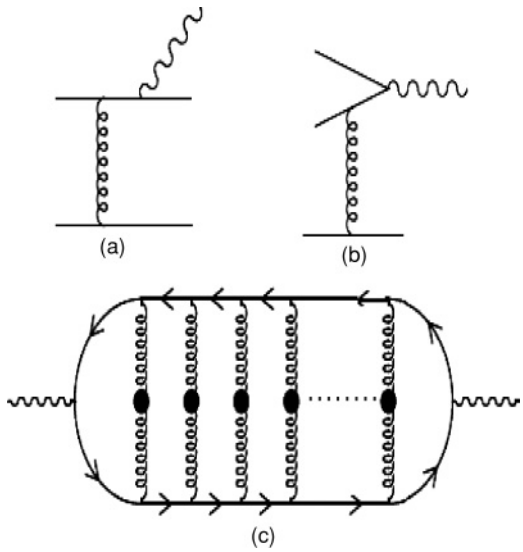

FIG. 1. Two-loop processes that contribute at order $\alpha\alpha_s$ to photon emission from (a) bremsstrahlung (b) AWS. Higher-loop processes having a ladder topology that contribute at the same order are shown in (c).

given in Eq. (5):

$$2\tilde{\mathbf{p}}_\perp = i\widetilde{\delta E}(\tilde{\mathbf{p}}_\perp, p_0, q_0, Q^2)\tilde{\mathbf{f}}(\tilde{\mathbf{p}}_\perp) + \int\frac{d^2\tilde{\ell}_\perp}{(2\pi)^2}\tilde{C}(\tilde{\ell}_\perp)[\tilde{\mathbf{f}}(\tilde{\mathbf{p}}_\perp) - \tilde{\mathbf{f}}(\tilde{\mathbf{p}}_\perp + \tilde{\ell}_\perp)] \tag{3}$$

$$\widetilde{\delta E} = \frac{q_0 T}{2p_0(q_0+p_0)}(\tilde{p}_\perp^2 + \kappa_{\rm eff}) \tag{4}$$

$$\tilde{C}(\tilde{\ell}_\perp) = \frac{1}{\tilde{\ell}_\perp^2} - \frac{1}{(\tilde{\ell}_\perp^2+1)} \tag{5}$$

In addition to transverse part, one needs to consider the longitudinal mode for the virtual photon emission. The corresponding longitudinal function is determined by the AGMZ integral equation [Eq. (6)], as derived in Ref. [23]:

$$2\sqrt{\frac{|p_0r_0|}{m_D^2}} = i\widetilde{\delta E}(\tilde{\mathbf{p}}_\perp, p_0, q_0, Q^2)\tilde{g}(\tilde{\mathbf{p}}_\perp) + \int\frac{d^2\tilde{\ell}_\perp}{(2\pi)^2}\tilde{C}(\tilde{\ell}_\perp)[\tilde{g}(\tilde{\mathbf{p}}_\perp) - \tilde{g}(\tilde{\mathbf{p}}_\perp + \tilde{\ell}_\perp)]. \tag{6}$$

I. GENERALIZED EMISSION FUNCTIONS FOR PHOTON EMISSION

In the present work, we solved Eqs. (3) and (6) via the iterations method at a fixed photon energy of $q_0/T = 50$. Alternatively, these equations can also be solved by variational approach [25]. In the following calculations, we used two flavors and three colors. Using the iterations method, we obtained $\mathbf{p}_\perp\cdot\mathbf{f}(\mathbf{p}_\perp)$, $g(\mathbf{p}_\perp)$ distributions for different p_0, q_0, Q^2, plasma temperatures ($T = 1.0, 0.50, 0.25$ GeV) and strong coupling constants ($\alpha_s = 0.30, 0.10, 0.05$). We integrate these $\mathbf{p}_\perp\cdot\mathbf{f}(\mathbf{p}_\perp)$, $g(\mathbf{p}_\perp)$ distributions to derive $I^{b,a}_{T,L}$ as defined in the Eqs. (7) and (8). The superscripts b, a in these equations

represent bremsstrahlung or AWS processes depending on the p_0 value used. The subscripts T, L represent contributions from transverse $[\mathbf{f}(\mathbf{p}_\perp)]$ or longitudinal $[g(\mathbf{p}_\perp)]$ parts. $I^{b,a}_{T,L}$ are the quantities required for calculating imaginary part of polarization tensor [see Eq. (2)].

$$I^{b,a}_T = \int \frac{\mathbf{d^2\tilde{p}}_\perp}{(2\pi)^2} \tilde{\mathbf{p}}_\perp \cdot \Re \tilde{\mathbf{f}}(\tilde{\mathbf{p}}_\perp) \tag{7}$$

$$I^{b,a}_L = \int \frac{\mathbf{d^2\tilde{p}}_\perp}{(2\pi)^2} \Re \tilde{g}(\tilde{\mathbf{p}}_\perp). \tag{8}$$

In the remaining part of this work, we adopt the formulas and results of Ref. [24] (presented at $T = 1$ GeV, $\alpha_s = 0.30$), by suitably redefining the quantities for all temperatures and strong coupling constants. In Eqs. (9)–(12) we define four dimensionless variables. The factor $\alpha_s/0.3$ in these equations is required to match the definitions in the present work with those of Ref. [24]. The variable x_1 is the real photon dynamical variable [20]. For virtual photon emission from QGP, we present two more variables, $x_{T,L}$, given in Eqs. (13) and (14).

$$x_0 = \frac{|(p_0 + q_0)p_0|}{q_0 T}, \tag{9}$$

$$x_3 = \frac{q_0 T(\alpha_s/0.3)}{Q^2}, \tag{10}$$

$$x_1 = x_0 \frac{M^2_\infty}{m^2_D}, \tag{11}$$

$$x_2 = x_0 \frac{Q^2}{q_0 T(\alpha_s/0.3)}, \tag{12}$$

$$x_T = x_1 + x_2, \tag{13}$$

$$x_L = x_2. \tag{14}$$

$I^{b,a}_{T,L}$ are in general functions of $\{p_0, q_0, Q^2, T, \alpha_s\}$ and when plotted versus any of these p_0, q_0, Q^2, they exhibit no simple trends. Following Ref. [24], we define the generalized emission functions (GEF) $g^{b,a}_{T,L}$ in Eq. (15).

$$g^{b,a}_{T,L}(x_{T,L}) = I^{b,a}_{T,L} c^{b,a}_{T,L}. \tag{15}$$

The GEF are functions of only $x_{T,L}$ variables unlike $I^{b,a}_{T,L}$. These GEF $(g^{b,a}_{T,L})$ are obtained from corresponding $I^{b,a}_{T,L}$ values by multiplying with $c^{b,a}_{T,L}$ coefficient functions given in Eqs. (16)–(20). The quantities $x_{T,L}$ and $c^{b,a}_{T,L}$ in Eqs. (13), (14), and (16)–(20) are not definitions and these are found by a search for dynamical variables:

$$c^b_T = \frac{1}{x_1^2}, \tag{16}$$

$$c^a_T = \frac{1}{x_1^2} \frac{x_3}{1 + x_3} \text{ for } x_2 < 2.0, \tag{17}$$

$$c^a_T = \frac{1}{x_1 x_2} \text{ for } x_2 \geqslant 2.0, \tag{18}$$

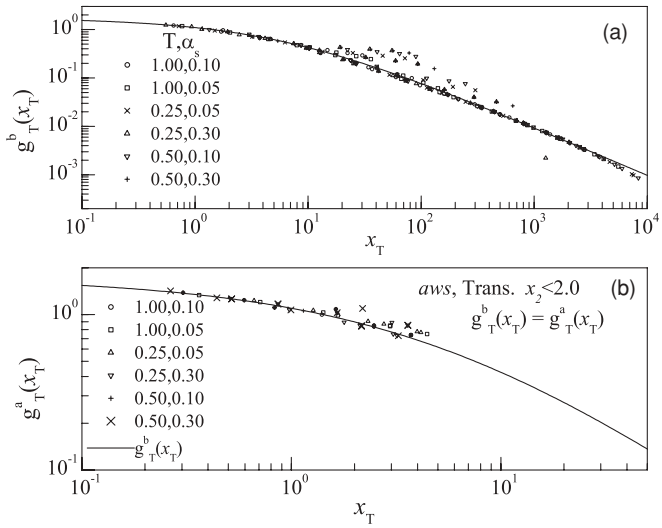

FIG. 2. (a) The dimensionless emission function $g^b_T(x)$ versus dynamical variable x_T defined in Eq. (13). Six cases of temperature and coupling constant values considered are mentioned in figure labels in different type symbols. The symbols represent the integrated values of $\mathbf{p}_\perp$ distributions as a function of $\{p_0, q_0, Q^2, T, \alpha_s\}$ values. These are transformed by c^b_T coefficient function given in Eq. (16). Essentially, various symbols merge and cannot be distinguished. The solid curve is an empirical fit given by Eq. (21). (b) The dimensionless emission function $g^a_T(x)$ versus dynamical variable x_T for $x_2 < 2.0$. The transformation coefficients c^a_T and empirical fits are given by Eqs. (17) and (22).

$$c^b_L = \frac{Q^2}{T^2(\alpha_s/0.3)} \left[\frac{T^2}{p_0(p_0 + q_0)}\right]^{\frac{3}{2}} \otimes \frac{\left(1.5 + x_3^{0.75}\right)}{x_2^{1/3}} \sqrt{\frac{\alpha_s}{0.3}}, \tag{19}$$

$$c^a_L = \frac{x_2^{0.10}}{x_1^{1.40}\sqrt{q_0/T}\left(1 + \sqrt{x_3}\right)} \sqrt{\frac{\alpha_s}{0.3}}. \tag{20}$$

Figure 2 shows the results for GEF for bremsstrahlung [Fig. 2(a)]. The calculations are performed for a fixed photon energy $(q_0/T = 50)$ but include six different cases of temperatures and coupling strengths mentioned in figure labels. The solid curve in Fig. 2(a) is the empirical fit to this emission function, given by Eq. (21).[1] The required c^b_T coefficient function is given in Eq. (16). It has been observed that for low Q^2, i.e., $x_2 < 2.0$, transverse part of AWS process behaves similar to the transverse bremsstrahlung function. Therefore, we transform the low Q^2 transverse part of AWS process as given by Eq. (17). The resulting emission function is shown in Fig. 1(b). The solid curve is the fit given in

[1]The fit given in Eq. (21) is an improvement over the result reported in Ref. [24].

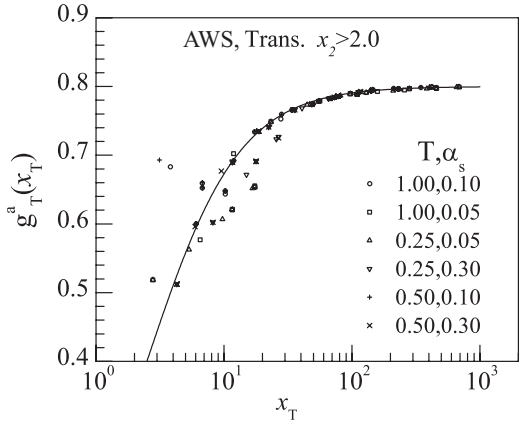

FIG. 3. The dimensionless emission function $g_T^a(x)$ versus dynamical variable x_T. The symbols are as in Fig. 2. Six different temperature and coupling constant values considered are mentioned in figure labels. The required c_T^a coefficient function is given in Eq. (18). The solid curve is an empirical fit given by Eq. (23).

Eq. (22), which is same as solid curve in Fig. 1(a).

$$g_T^b(x) = \frac{10.0}{5.6 + 2.5\sqrt{x} + x}, \tag{21}$$

$$g_T^a(x) = g_T^b(x) \quad \text{for} \quad x_2 < 2.0, \tag{22}$$

$$g_T^a(x) = \frac{0.80}{(1 + 3/x^{1.2})} \quad \text{for} \quad x_2 \geqslant 2.0, \tag{23}$$

$$g_L^b(x) = \frac{0.0876}{1 + (x/3.7727)^{1.18}}, \tag{24}$$

$$g_L^a(x) = 0.299803x^{0.5772} \quad \text{for} \quad x < 1.45, \tag{25}$$

$$g_L^a(x) = 1.04344 \ln(x) \quad \text{for} \quad x \geqslant 1.45. \tag{26}$$

The emission function for high Q^2 values ($x_2 > 2.0$) for transverse part of AWS process is shown in Fig. 3. The c_T^a and the emission function are given in Eqs. (18) and (23). Similarly, Figures 4(a) and 4(b) show the longitudinal components of GEF for bremsstrahlung [Fig. 4(a)] and AWS [Fig. 4(b)]. The coefficient functions and GEF are given in Eqs. (19), (20), (24), (25), and (26). These transformation functions are very complex.[2]

II. GEF AND PHOTON RETARDED POLARIZATION TENSOR

In the previous section, we used the results from the iterations method to obtain the $I_{T,L}^{b,a}$ values. We transformed these into GEF ($g_{T,L}^{b,a}$) functions shown in Figs. 2–4. We fitted these by empirical functions given in Eqs. (21)–(26). Using the empirical functions, for any $p_0, q_0, Q^2, T, \alpha_s$ values, we can generate the $I_{T,L}^{b,a}$ values. Hence, using GEF and the $c_{T,L}^{b,a}$, the imaginary part of photon retarded polarization tensor of

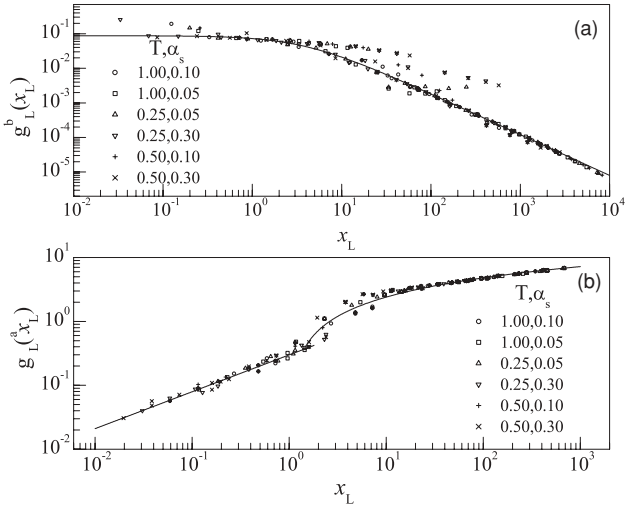

FIG. 4. (a) The dimensionless emission function $g_L^b(x)$ versus dynamical variable x_L defined in Eq. (14). The symbols represent the integrated values of $\mathbf{p}_\perp$ distributions as a function of $\{p_0, q_0, Q^2, T, \alpha_s\}$ values. These are transformed by c_L^b coefficient function given in Eq. (19). The solid curve is an empirical fit given by Eq. (24). The temperature and coupling constant values are shown in different type symbols, as mentioned in figure labels. (b) The dimensionless emission function $g_L^a(x)$ versus dynamical variable x_L. The transformation coefficients c_L^a and empirical fit are given by Eqs. (20), (25), and (26).

Eq. (2) can be written as [24][3]

$$\Im\Pi_{R\mu}^{\mu} = \frac{e^2 N_c}{2\pi} \int_{-\infty}^{\infty} dp_0 [n_F(r_0) - n_F(p_0)] \otimes (Tm_D^2) \left[\frac{p_0^2 + r_0^2}{2(p_0 r_0)^2} \left(\frac{g_T^i(x_T)}{c_T^i} \right) + \frac{1}{\sqrt{|p_0 r_0|}} \frac{Q^2}{q^2} \left(\frac{1}{m_D} \right) \left(\frac{g_L^i(x_L)}{c_L^i} \right) \right]. \tag{27}$$

Here, the superscript i denotes $\{b, a\}$ depending on the value of the integration variable p_0. We have calculated imaginary photon polarization tensor and dilepton emission rates using Eq. (27) and made a detailed comparison with the results of Ref. [23]. For this comparison, we generated reference results using the program provided in Ref. [27], which interpolates from a table of precompiled exact numerical results. The agreement of the GEF method [Eq. (27)] with the results of Ref. [27] was observed to be very good. As an example, we show the dilepton emission rates in Fig. 5. Figure 5(a) shows the GEF results represented by symbols compared with the results of Ref. [27] represented by solid lines at two photon energies. The GEF results for $q_0/T = 20.0$ (circles) were generated using $\alpha_s = 0.05$, $T = 1.0$ GeV and for $q_0/T = 10.0$ (triangles) results were generated using $\alpha_s = 0.30$, $T = 0.25$ GeV. Similarly in Fig. 5(b) we show the rates from GEF method for

[2]The Eqs. (19), (20), (25), and (26) are slightly different from the corresponding equations presented in Ref. [24].

[3]The factor T in (Tm_D^2) in Eq. (27) is arising from the tilde transformation. This extra T cancels the temperature in m_D/T factor coming from tilde transformation of f, g functions. This T was missing in Ref. [24].

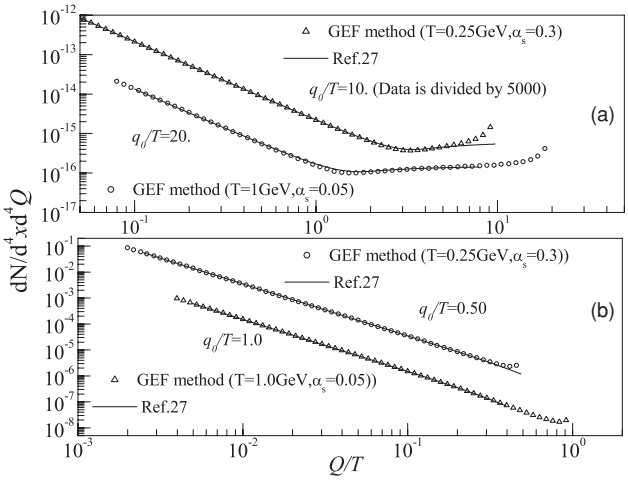

FIG. 5. (a and b) Dilepton emission rates using GEF method shown in symbols and compared with results of Ref. [27] represented by solid lines. All the details are mentioned in figure labels and text. The rates plotted are divided by T^2.

$q_0/T = 0.50$ (circles) generated using $\alpha_s = 0.30$, $T = 0.25$ GeV and for $q_0/T = 1.0$ (triangles) using $\alpha_s = 0.05$, $T = 1.0$ GeV. The agreement of GEF method with lines is seen to be very good, except at the highest values of Q/T. This deviation is caused because for the longitudinal part in Eq. (27), we used photon momentum Q^2/q^2. When this is replaced with photon energy Q^2/q_0^2 as shown in Eq. (28), the agreement of our results with those of Ref. [27] is very good in the full range of Q/T. In the remaining part of this article, we use only Eq. (28).

$$\Im\Pi^{\mu}_{R\mu} = \frac{e^2 N_c}{2\pi}\int_{-\infty}^{\infty} dp_0[n_F(r_0) - n_F(p_0)] \otimes \left(T m_D^2\right)\left[\frac{p_0^2 + r_0^2}{2(p_0 r_0)^2}\left(\frac{g_T^i(x_T)}{c_T^i}\right) + \frac{1}{\sqrt{|p_0 r_0|}}\frac{Q^2}{q_0^2}\left(\frac{1}{m_D}\right)\left(\frac{g_L^i(x_L)}{c_L^i}\right)\right]. \quad (28)$$

We will present more results in a different way by defining reduced quantities. After obtaining the $\Im\Pi^{\mu}_{R\mu}$ versus Q^2, q_0, T, α_s by using Eq. (28), we define $Q_{\rm red}$ and reduced polarization tensor as in Eqs. (29) and (30). The reduced polarization tensors are calculated for different photon energies, different coupling strengths and temperatures. We plotted these results in black circles in Figs. 6 and 7 (also in Figs. 10 and 11, to be discussed later) versus $Q_{\rm red}$. For comparison, results from Ref. [27] are shown in triangles. The agreement of these two symbols is seen to be very good from low to very high photon energies, $q_0/T \sim 0.05$–50.0.

$$Q_{\rm red} = \frac{Q}{T}\sqrt{\frac{0.3}{\alpha_s}} \quad (29)$$

$$\Im\Pi_{\rm red} = \frac{\Im\Pi^{\mu}_{R\mu}(Q^2, q_0, T, \alpha_s)}{T^2}\left(\frac{0.30}{\alpha_s}\right) \quad (30)$$

$$\Im\Pi_{\rm red} = F\left(Q_{\rm red}, \frac{q_0}{T}\right). \quad (31)$$

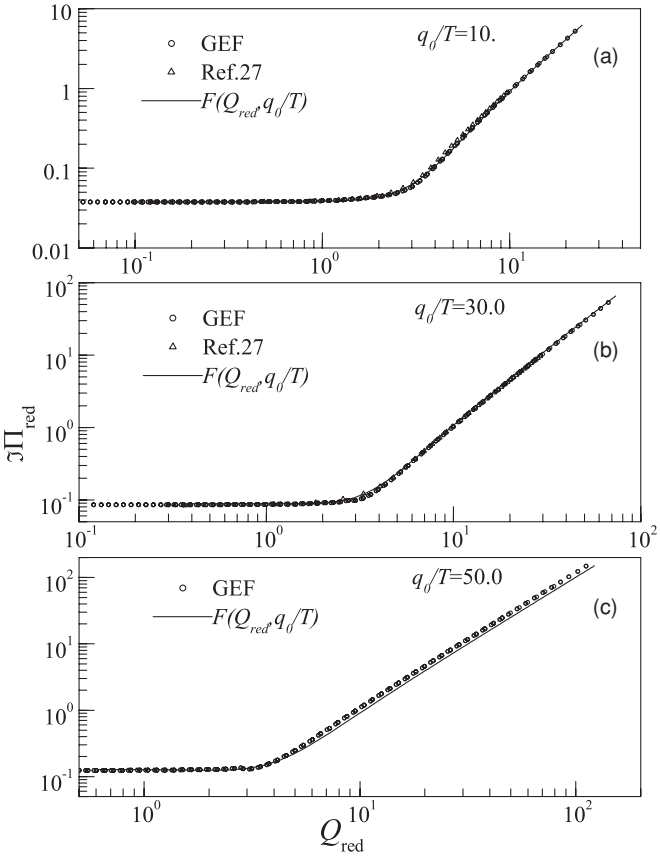

FIG. 6. $\Im\Pi_{\rm red}$ plotted as a function of $Q_{\rm red} = \frac{Q}{T}\sqrt{\frac{0.3}{\alpha_s}}$ for various photon energies (q_0/T) mentioned in figure. The imaginary polarization tensor includes all contributions from transverse components of bremsstrahlung, AWS, and also from the corresponding longitudinal parts. The black circles represent the GEF method in Eq. (28). The triangles represent the results of Ref. [27]. The solid lines represent the results using Eq. (36).

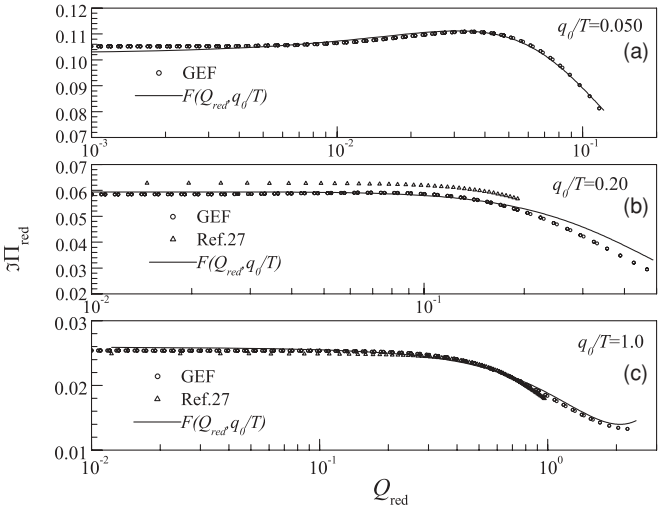

FIG. 7. $\Im\Pi_{\rm red}$ plotted as a function of $Q_{\rm red}$ for low q_0/T values mentioned in figure. The details are as in the Fig. 6.

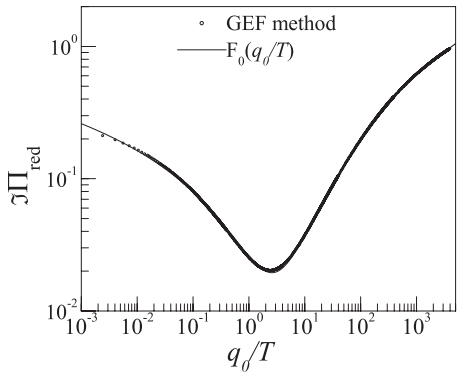

FIG. 8. The reduced imaginary part of polarization tensor defined in Eq. (30), versus q_0/T. We have taken $Q \sim 10^{-4} q_0$. Solid curves are fits given in Eqs. (33) and (34). Symbols represent the results from GEF method using Eq. (28).

III. PHENOMENOLOGY USING GENERALIZED EMISSION FUNCTIONS

The two-loop processes along with the LPM effects contribute significantly to dilepton emission rates from QGP, at low as well as high photon Q^2 values. This aspect was discussed in detail in Refs. [23,24] by comparing the contributions (to $\Im\Pi^{\mu}_{R\mu}$) from the one-loop and higher-loop processes. Further as mentioned in the Introduction, dilepton emission from the radiating jets also contributes to experimental dilepton yields [8]. There are simple empirical formulas available for the dilepton emission rates at the one-loop level [21]. In this section, we obtain the phenomenological fits to virtual photon emission rates from QGP for ladder processes with LPM effects. We will provide simple phenomenological formulas that will be useful in model calculations for experimental dilepton yields. We will show a comparison of $\Im\Pi^{\mu}_{R\mu}$ from our phenomenological formulas with the numerical results of

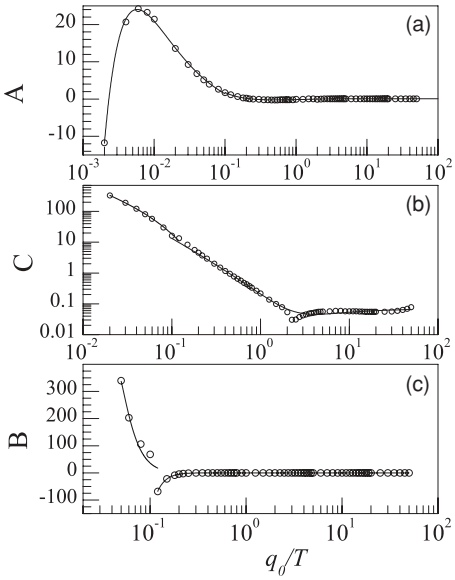

FIG. 9. The A, B, and C parameters versus q_0/T. The curves represent fits by suitable functional forms in Eqs. (37), (40), and (42) discussed in text. These are useful to generate Π_{red} using Eq. (36).

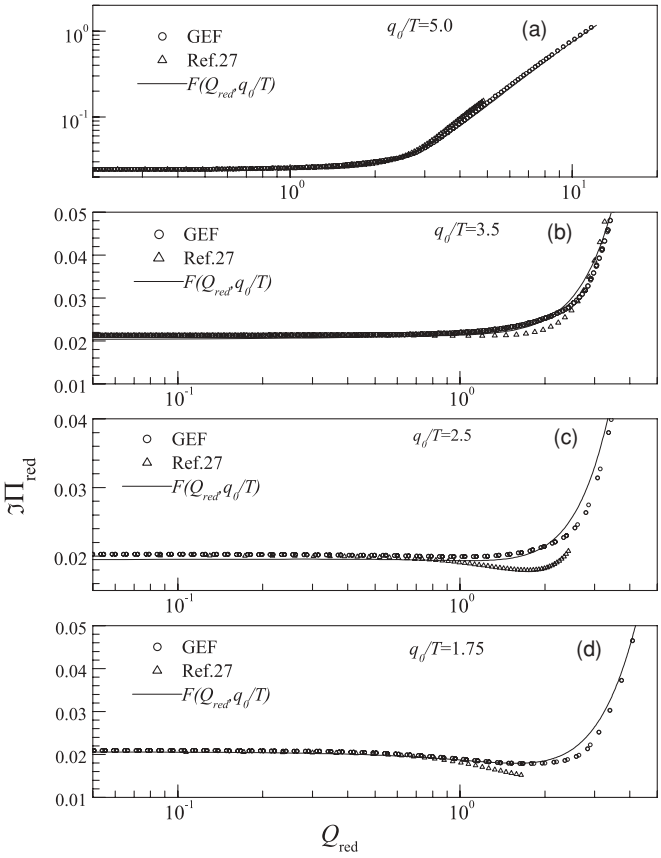

FIG. 10. $\Im\Pi_{red}$ plotted as a function of Q_{red} for low q_0/T values mentioned in figure. The details are as described in the caption to Fig. 6.

Ref. [27]. From Figs. 6 and 7, it is clear that the reduced quantities depend on only two variables, i.e., instead of $\{Q^2, q_0, T, \alpha_s\}$, we need only $\{Q_{red}, q_0/T\}$ to generate Π_{red} as in Eq. (31). This observation was already reported in Ref. [23]. To study this $F(Q_{red}, q_0/T)$ in detail, we use Eq. (28) to generate imaginary part of polarization tensor for various values of Q^2, q_0, T, α_s. We observed that in the limit of $Q_{red} \to 0$; $F(Q_{red}, \frac{q_0}{T}) \to F_0(\frac{q_0}{T})$ as given by Eq. (32) and this limit is true for any q_0/T. Further, as given by Eq. (33), for $q_0/T < 0.020$; $F(Q_{red}, \frac{q_0}{T}) \approx F_0(\frac{q_0}{T})$ for any allowed Q_{red}. Therefore, $F_0(x)$ is an important function for virtual photon emission, as this function arises in two different limits [see Eqs. (32) and (33)].

$$F(Q_{red}, x) \to F_0(x) \quad \text{as} \quad Q_{red} \to 0 \tag{32}$$

$$F(Q_{red}, x) \approx F_0(x) \quad \text{for} \quad x \leqslant 0.020 \tag{33}$$

$$x = \frac{q_0}{T}.$$

To obtain this $F_0(x)$, we generate the $\Im\Pi$ at a very low Q^2 for various values of $q_0/T, \alpha_s$. Using the results, we construct $Q_{red}, \Im\Pi_{red}$. The results are shown in Fig. 8 by symbols labeled GEF method. We fitted this data by suitable functions as given in Eqs. (34) and (35) (along with their parameters). These are two different fits, for q_0/T <200 and for q_0/T >100, with an overlap between 100 and 200 (where both fits are good). These

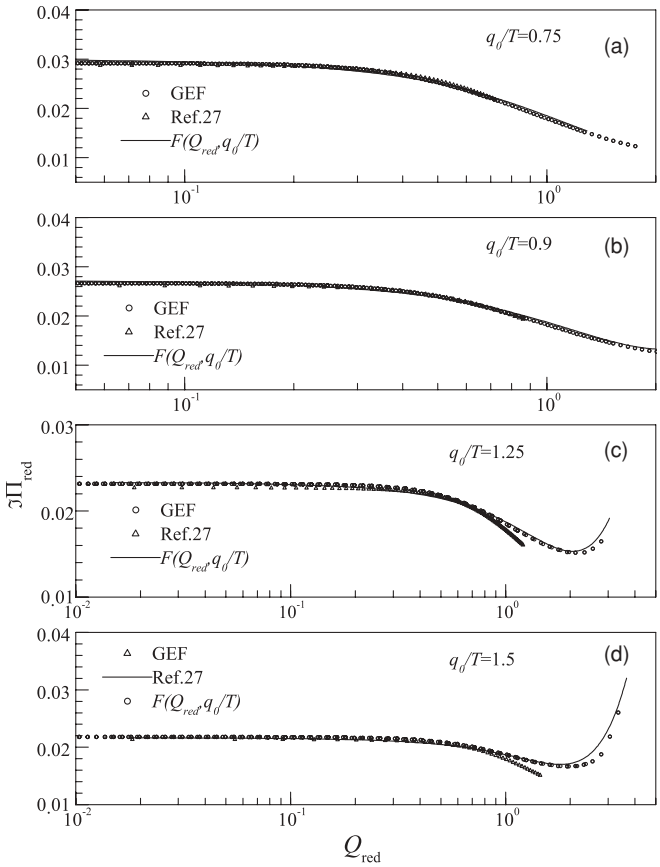

FIG. 11. $\Im\Pi_{\rm red}$ plotted as a function of $Q_{\rm red}$ for low q_0/T values mentioned in figure. The details are as in the Fig. 6.

fits are represented by solid curves and labeled F_0 in figure.

$$\begin{aligned} F_0(x) &= a + bx^{p_1} + \frac{c}{\sqrt{x^{p_2}}} \quad \text{for} \quad x \leqslant 200, \\ a &= -2.99077, \\ b &= 0.0791399, \\ c &= 2.93755, \\ p_1 &= 0.371976, \\ p_2 &= 0.0288541, \end{aligned} \tag{34}$$

$$\begin{aligned} F_0(x) &= a + b\sqrt{x^p} \quad \text{for} \quad x \geqslant 100.0, \\ a &= -0.474129, \\ b &= 0.255163, \\ p &= 0.419646. \end{aligned} \tag{35}$$

For the case of finite Q, we made empirical fits by choosing a function given in Eq. (36). In this equation, the A, B, and C parameters are functions of q_0/T. These parameters are determined by fitting the Q plots for various q_0/T, obtained from Eq. (28). The parameters values for various q_0/T are tabulated and the results are shown in Fig. 9 by symbols. It is very important to have an empirical formula to generate A, B, and C values.

$$F(Q_{\rm red}, x) = F_0(x)\frac{1 + A(x)Q_{\rm red} + B(x)Q_{\rm red}^4}{1 + C(x)Q_{\rm red}^2}. \tag{36}$$

TABLE I. Values of the a, b, c, p_1, p_2 parameters are listed for $A(x)$, $B(x)$, $C(x)$ of Eqs. (37)–(44) in different x regions.

$A(x)$	$x \leqslant 0.1$	$0.1 < x \leqslant 3.5$	
a	−4.84554727516	0.33219586043	
b	1.478772613744	1.34926189543	
c	0.4963049612794	1.82125018461	
p_1	−0.93213485133	−1.0422409717	
p_2	−1.1101191721	−0.86799168105	
	$A(x) = A(3.5)$	for $x > 3.50$	
$B(x)$	$x \leqslant 0.20$	$0.2 < x \leqslant 1.0$	$x > 1.0$
a	−0.132747	0.012385	−0.0454930477
b	0.0661859	0.0924141	0.1940150437
c	0.0642336	0.0878252	0.1372510415
p_1	−4.76869	−4.18536	−0.237037465
p_2	−4.77762	−4.25575	−0.42563026
$C(x)$	$x \leqslant 0.15$	$x > 0.15$	
a	7.48658946052	0.0692890486	
b	13.1687711578	0.945340977	
c	19.9115694165	0.8057948943	
p_1	−1.0750505095	−1.4427187803	
p_2	−0.8514587339	−1.2054627582	

Therefore, these A, B, C parameters were fitted by different functional forms as given in Eqs. (37), (40), and (42). The fits are given for different q_0/T regions as shown in Eqs. (37)–(44) and these parameters are listed in Table I for convenience. Depending on the requirement, one can select the relevant parameter set to generate A, B, and C values.[4] Apparently in Fig. 9, at high q_0/T (beyond 0.10), these parameters are constant, however this is very misleading. The present fits generate quite well even the small variations of these parameters over full region. Good quality A, B, C fits are required because the Q plots are sensitive to these parameters. Further, the A, B, C parameter fits are given only up to $q_0/T = 50.0$. Therefore, extrapolation beyond this q_0/T may not be valid unless confirmed using Eq. (28). Using these formulas we get A, B, C coefficients (up to $q_0/T = 50.0$) and we get $F_0(x)$ from Eqs. (34) and (35). We use these in Eq. (36) to generate $\Im\Pi_{\rm red}$. These phenomenological results are shown by solid curves in Figs. 6, 7, 10, and 11.

$$\begin{aligned} A(x) &= a + (bx^{p_1} - cx^{p_2}) \quad \text{for} \quad x \leqslant 0.1, \\ a &= -4.84554727516, \\ b &= 1.478772613744, \\ c &= 0.4963049612794, \\ p_1 &= -0.93213485133, \\ p_2 &= -1.1101191721, \end{aligned} \tag{37}$$

[4]It should be noted that for A, B, C fits, the functional forms have difference of power law and hence demand high precision of their parameters. Therefore, one should not truncate these parameters, especially the power exponents given by p, p_1, p_2.

$$
\begin{aligned}
&A(x) \qquad \text{for} \quad 0.1 < x \leqslant 3.5, \\
&\quad a = 0.33219586043, \\
&\quad b = 1.34926189543, \\
&\quad c = 1.82125018461, \\
&\quad p_1 = -1.0422409717, \\
&\quad p_2 = -0.86799168105,
\end{aligned} \tag{38}
$$

$$
A(x) = A(3.5) \quad \text{for} \quad x > 3.50. \tag{39}
$$

$$
\begin{aligned}
&C(x) = a + (bx^{p_1} - cx^{p_2}) \quad \text{for} \quad x \leqslant 0.15, \\
&\quad a = 7.48658946052, \\
&\quad b = 13.1687711578, \\
&\quad c = 19.9115694165, \\
&\quad p_1 = -1.0750505095, \\
&\quad p_2 = -0.8514587339,
\end{aligned} \tag{40}
$$

$$
\begin{aligned}
&C(x) \qquad \text{for} \quad x > 0.15, \\
&\quad a = 0.0692890486, \\
&\quad b = 0.945340977, \\
&\quad c = 0.8057948943, \\
&\quad p_1 = -1.4427187803, \\
&\quad p_2 = -1.2054627582,
\end{aligned} \tag{41}
$$

$$
\begin{aligned}
&B(x) = a + (bx^{p_1} - cx^{p_2}) \quad \text{for} \quad x \leqslant 0.20, \\
&\quad a = -0.132747, \\
&\quad b = 0.0661859, \\
&\quad c = 0.0642336, \\
&\quad p_1 = -4.76869, \\
&\quad p_2 = -4.77762,
\end{aligned} \tag{42}
$$

$$
\begin{aligned}
&B(x) \qquad \text{for} \quad 0.2 < x \leqslant 1.0, \\
&\quad a = 0.012385, \\
&\quad b = 0.0924141, \\
&\quad c = 0.0878252, \\
&\quad p_1 = -4.18536, \\
&\quad p_2 = -4.25575,
\end{aligned} \tag{43}
$$

$$
\begin{aligned}
&B(x) \qquad \text{for} \quad x > 1.0, \\
&\quad a = -0.0454930477, \\
&\quad b = 0.1940150437, \\
&\quad c = 0.1372510415, \\
&\quad p_1 = -0.237037465, \\
&\quad p_2 = -0.42563026.
\end{aligned} \tag{44}
$$

In conclusion, the photon emission rates from the quark-gluon plasma have been studied as a function of photon mass, considering LPM effects at various temperatures and strong coupling strengths. We defined generalized dynamical variables x_T, x_L for transverse and longitudinal components of bremsstrahlung and AWS mechanisms. In addition, we defined generalized emission functions (GEF), namely $g_T^b(x_T)$, $g_T^a(x_T)$, $g_L^b(x_L)$, $g_L^a(x_L)$. We have obtained empirical fits to these GEF. In terms of the GEF, we have calculated the imaginary part of retarded photon polarization tensor as a function of photon energy and mass, plasma temperature, and strong coupling strengths. For phenomenological applications, we fitted the reduced imaginary polarization tensor by simple functions and provided necessary parameters. These empirical formulas will be useful in model calculations for experimental dilepton yields.

ACKNOWLEDGMENTS

I am thankful to S. V. Ramalakshmi for cooperation during this work.

[1] F. Karsch, Nucl. Phys. **A698**, 199 (2002).
[2] I. Arsene *et al.* (BRAHMS Collaboration), Nucl. Phys. **A757**, 1 (2005), [nucl-ex/0410020v1].
[3] B. B. Back *et al.* (PHOBOS Collaboration), Nucl. Phys. **A757**, 28 (2005).
[4] J. Adams *et al.* (STAR Collaboration), Nucl. Phys. **A757**, 102 (2005).
[5] K. Adcox *et al.* (PHENIX Collaboration), Nucl. Phys. **A757**, 184 (2005).
[6] G. David, R. Rapp, and Z. Xu, nucl-ex/0611009v2.
[7] David d'Enterria, J. Phys. G **34**, S53 (2007), topical review.
[8] S. Turbide and C. Gale, J. Phys. G **34**, S1019 (2007).
[9] F. Karsch, E. Laermann, P. Petreczky, S. Stickan, and I. Wetzorke, Phys. Lett. **B530**, 147 (2002).
[10] F. Karsch, S. Datta, E. Laermann, P. Petreczky, S. Stickan, and I. Wetzorke, Nucl. Phys. **A715**, 701 (2003).
[11] J.-P. Blaizot1 and F. Gelis, Eur. Phys. J. C **43**, 375 (2005), [hep-ph/0504144].
[12] F. Arleo *et al.*, hep-ph/0311131v3, Chap. 4 of CERN Yellow Report CERN-2004-009-D (Geneva, Switzerland, 2004), p. 367.
[13] S. Gupta, Phys. Lett. **B597**, 57 (2004).
[14] E. Braaten and R. D. Pisarski, Nucl. Phys. **B337**, 569 (1990).

[15] G. D. Moore and J.-M. Robert, hep-ph/0607172.
[16] L. D. Landau and I. Ya. Pomeranchuk, Dokl. Akad. Nauk SSR **92**, 535 (1953); **92**, 735 (1953).
[17] A. B. Migdal, Phys. Rev. **103**, 1811 (1956).
[18] P. Arnold, G. D. Moore, and Laurence G. Yaffe, J. High Energy Phys. 11 (2001) 057.
[19] P. Arnold, G. D. Moore, and Laurence G. Yaffe, J. High Energy Phys. 12 (2001) 009.
[20] S. V. S. Sastry, Phys. Rev. C **67**, 041901(R) (2003).
[21] T. Altherr and P. V. Ruuskanen, Nucl. Phys. **B380**, 377 (1992).
[22] M. H. Thoma and C. T. Traxler, Phys. Rev. D **56**, 198 (1997), [hep-ph/09701354].
[23] P. Aurenche, F. Gelis, G. D. Moore, and H. Zaraket, J. High Energy Phys. 12 (2002) 006.
[24] S. V. Suryanarayana, Phys. Rev. C **75**, 021902(R) (2007).
[25] S. V. Suryanarayana, hep-ph/0609096.
[26] P. Aurenche, F. Gelis, and H. Zaraket, J. High Energy Phys. 05 (2002) 043 .
[27] F. Gelis, libLPM-v1, http://www.spht.cea.fr/Images/Pisp/fgelis/Soft/LPM/v1/Readme_v1.php.